Check for updates

www.afm-journal.de

One-Step Sintering Synthesis Achieving Multiple Structure Modulations for High-Voltage LiCoO₂

Hengyu Ren, Wenguang Zhao, Haocong Yi, Zhefeng Chen, Haocheng Ji, Qi Jun, Wangyang Ding, Zijian Li, Mingjie Shang, Jianjun Fang, Ke Li, Mingjian Zhang, Shunning Li,* Qinghe Zhao,* and Feng Pan*

The structure instability issues of the highly delithiated $LiCoO_2$ have significantly hindered its high-voltage applications (\geq 4.55 V vs Li/Li^+). Herein, for the first time, multiple modifications of $Li_{0.9}Mg_{0.05}CoO_2$ ($L_{0.9}M_{0.05}CO$) via a simple one-step sintering synthesis are reported. A combination of the bulk Li/Co antisites, a Mg-pillar enriched surface, and a thin Mg–O coating layer is achieved to maintain both the bulk and surface structural stability of $L_{0.9}M_{0.05}CO$ upon cycling at an upper cut-off voltage of 4.6 V. The bulk Li/Co antisites are discovered to enhance the H1-3 phase evolution reversibility, the Mg pillars that substitute the Li sites effectively reinforces the surface structure, and the thin Mg–O coating layer can effectively prevent the cathode from severe side reactions. Benefiting from the reduced but reversible H1-3 phase transition and the reinforced surface structure, $L_{0.9}M_{0.05}CO$ shows an excellent cycle stability. This work provides a new structure modulation route for developing high-voltage $LiCoO_2$ cathodes.

1. Introduction

In the past three decades, LiCoO₂ (LCO) has been exploited as a promising cathode material and commercialized in the portable electronics market due to its high volumetric energy/power density, easy preparation, and excellent reliability. To meet the growing demands for high-energy-density Li-ion batteries, substantial endeavors have been made to increase the cut-off voltage for achieving higher capacity of LCO. However, serious

H. Ren, W. Zhao, H. Yi, Z. Chen, H. Ji, W. Ding, Z. Li, M. Shang, J. Fang, K. Li, M. Zhang, S. Li, Q. Zhao, F. Pan School of Advanced Materials Peking University Shenzhen Graduate School Shenzhen 518055, China E-mail: lisn@pku.edu.cn; zhaoqh@pku.edu.cn; panfeng@pkusz.edu.cn Q. Jun School of Materials Sun Yat-Sen University Shenzhen 518107, China M. Zhang School of Science and Engineering The Chinese University of Hong Kong

(D)

The ORCID identification number(s) for the author(s) of this article can be found under https://doi.org/10.1002/adfm.202302622

DOI: 10.1002/adfm.202302622

Shenzhen 518172, China

structural and interfacial instability issues emerge when elevating the charge voltage up to \geq 4.5 V versus Li/Li⁺.^[1] In particular, the H1-3 phase transition near \approx 4.55 V induce obvious sliding of the O–Co–O slabs, accompanied with lithium rearrangement and volume shrinkage along c-axis, causing pernicious structural evolution and particle crack propagation.^[2] Moreover, the highly oxidative Co⁴⁺ and Oⁿ⁻ (n < 2) under high voltage leads to severe surface side reactions accompanied with oxygen loss and Co dissolution, which further triggers collapse of lattice structure and damage of morphology, resulting in dramatic capacity fading.^[3]

To break through the bottleneck of ≥4.55 V, multiple modifications have been proposed to modify both bulk and surface structures, such as elemental doping, surface structure enhancement, and rational choice of electrolyte additives.^[4] In terms

of materials structure modulations methods, a durable structure of LCO can be achieved by the following factors: the "pillar" effect from elemental doping, [1,3b,5] the formation of robust surface spinel/rock salt (S/R) buffering region, [6] the application of appropriate surface coating, [7] and the substitution of surface-active O species. [8]

Recently, the "pillar" effect of Mg, [5a-d] Ln, [5e] and Rb, [7a] occupying in the Li sites, have been demonstrated to suppress structure collapse along the *c*-axis. This kind of "pillar" effect contributes to the formation of flat Co–O layers, especially in the vicinity of the surface, which is identified as the origin for the enhanced cycling stability of the high-voltage LCO, as confirmed by our previous studies. [9] Notably, the "pillar" effect which exists in both bulk and surface regions, can effectively reduce the irreversible O–Co–O slabs sliding, i.e., the detrimental H1–3 phase transitions, and thus both the bulk and surface structure can be well-maintained upon high voltage. Meanwhile, the surface Li/Co antisites, which could be regarded as the "pillar" effect of Co, they play an effective role in accommodating the internal stress and stabilizing the active lattice oxygen. [10]

Introduction of the structurally robust S/R buffering region, no matter upon synthesis or during electrochemical operation, can generally reinforce the surface structural stability.^[6a] This benefit is mainly attributed to the reduced tendency of oxidation for the lattice oxygen ions in S/R phases when compared with that

16163028, 2023, 38, Downloaded from https://adv

anced.onlinelibrary.wiley.com/doi/10.1002/adfm.202302622 by University Town Of Shenzhen, Wiley Online Library on [23/11/2025]. See the Terms and Conditions

ditions) on Wiley Online Library for rules of use; OA articles are governed by the applicable Creative Commons

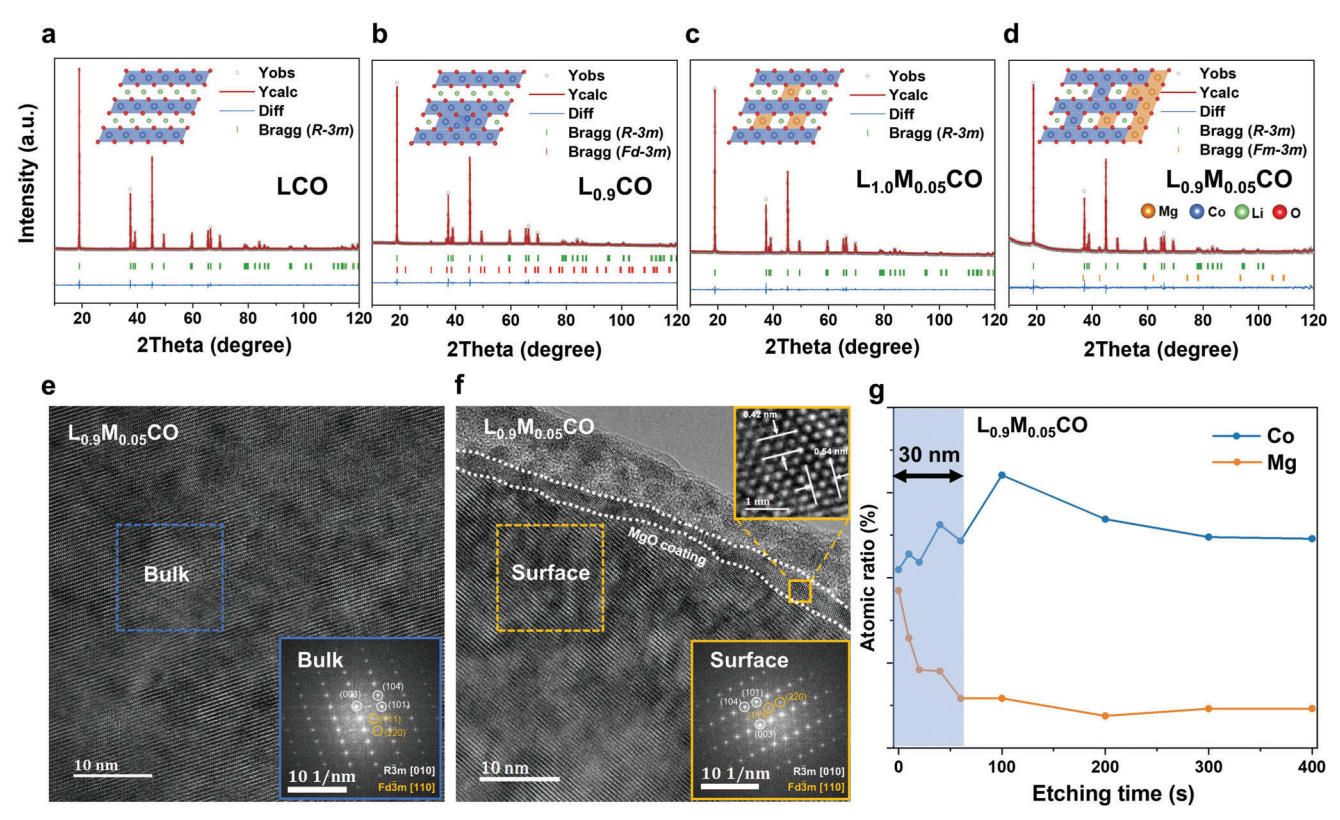


Figure 1. a–d) Rietveld refinements of the XRD patterns and schematic structure for LCO, $L_{0.9}$ CO, $L_{1.0}$ M $_{0.05}$ CO, and $L_{0.9}$ M $_{0.05}$ CO. f,g) HRTEM image of bulk and surface structure of $L_{0.9}$ M $_{0.05}$ CO. The inset FFT image indicates a layer/spinel hybrid structure. h) Element atomic concentrations of Co and Mg in $L_{0.9}$ M $_{0.05}$ CO from surface to interior obtained from XPS result.

in layer structure. [6f] Besides, this S/R phases can alleviate the lattice mismatch between the bulk phase and the coating layer, thus facilitating Li⁺ ion transport at the interface.^[6b,c,11] Our previous work has revealed the formation of surface spinel buffering region due to the surface gradient anion- and cation-doping, and similar results have also been demonstrated in other studies. showing that surface spinel can prevent oxygen migration out of the LCO particle at high voltages.[8a,12] Moreover, the coating layer can mitigate the direct contact between the active cathode material and the electrolyte, which could eliminate the issue of side reactions.^[7b-e] Also, the surface structure can be reinforced via substituting the lattice oxygen with F and/or Se, which effectively reduces the formation of highly oxidative On- species at high voltage. [5d,8] The surface coating layer can further help establish a structurally robust F-rich CEI, which can significantly stabilize the surface structure of LCO electrode.[13]

Overall, a durable high-voltage LCO electrode calls for the combination of reinforced bulk and surface structures. [5c,d,14] To achieve this goal, previous attempts have been focused on LCO coating by means of wet chemistry and re-sintering treatment, which is too expensive for industrialization. Herein, we demonstrate a cost-effective one-step sintering approach to achieve multiple modifications of LCO electrode, including introduction of Li/Co antisites, Mg-pillar enriched surface and a thin protective Mg-O coating layer. In particular, the Li/Co antisites help stabilize the bulk phase and impose high reversibility for the structure transition to H1-3 phase upon cycling at a high cut-off volt-

age of 4.6 V. The formation of the Mg-pillar enriched surface and Mg-O coating layer can, on the other hand, hinder the detrimental phase transition from surface into core, and reduce the side reaction via forming F-rich CEI. All the above benefits contribute to the enhanced cycling stability of high-voltage LCO at 4.6 V.

2. Results and Discussion

2.1. Structure Characterizations

All the LiCoO2 samples studied in this work are synthesized via mixing the MgO, Li₂CO₃, and Co₃O₄ reactants based on the designed stoichiometric ratios, then sintering at 900 °C for 12 h in an air atmosphere. We design four kinds of samples with various characters, i.e., the pristine LiCoO₂ (LCO), Li_{0.9}CoO₂ with Li deficiency ($L_{0.9}CO$), $Li_{1.0}Mg_{0.05}CoO_2$ with Mg dopants ($L_{1.0}M_{0.05}CO$), Li_{0.9}Mg_{0.05}CoO₂ with both the Li deficiency and Mg dopants $(L_{0.9}M_{0.05}CO)$. The synthesized materials show similar morphology with D_{50} of about $\approx 4.5 \, \mu \text{m}$, mainly due to the size of the pristine Co₃O₄ precursors (Figure S1, Supporting Information). ICP results in Table S1 (Supporting Information) show the successful doping of Mg elements in both $L_{0.9}M_{0.05}CO$ and $L_{1.0}M_{0.05}CO$. Comparing the XRD refinement results (Figure 1a-d; Tables S3-S6, Supporting Information) and TEM results (Figure 1e,f; Figures S2-S5, Supporting Information), we find that, in $L_{0.9}CO$ and $L_{0.9}M_{0.05}CO$, Li deficiency leads to the incomplete

ADVANCED FUNCTIONAL MATERIALS 16163028, 2023, 38, Downloaded

anced.onlinelibrary.wiley.com/doi/10.1002/adfm.202302622 by University Town Of Shenzhen, Wiley Online Library on [23/11/2025]. See the Terms and Conditions (https://

and-conditions) on Wiley Online Library for rules of use; OA articles are governed by the applicable Creative Commons

 Table 1. Illustrating the structure features of four samples.

transformation from spinel-type Co_3O_4 to layered LiCoO_2 , and therefore a layer/spinel hybrid structure is obtained.^[15]

It is worth noting that the above-mentioned spinel parts in bulk structures of $L_{0.9}CO$ and $L_{0.9}M_{0.05}CO$ includes both the Co₃O₄ domains and Li/Co antisites. Without adding MgO, both Co_3O_4 domains and Li/Co antisites emerge in the bulk of $L_{0.9}CO$, while for L_{0.9}M_{0.05}CO, only the Li/Co antisites are detected. HAADF-STEM results show that the Li/Co antisites are homogenously distributed in the interior of L_{0.9}M_{0.05}CO within a region of <5 nm in diameter (Figure S6, Supporting Information). In other words, the Li/Co antisites can be regarded as the ultrafine spinel domains to stabilize the layer structure of L_{0.9}M_{0.05}CO. By comparing the TEM results of L_{0.9}CO and L_{0.9}M_{0.05}CO, we find that the characteristic electron diffraction spots for the spinel parts are brighter in $L_{0.9}CO$ than that in $L_{0.9}M_{0.05}CO$ (Figure S3, Supporting Information; Figure 1e,f). This indicates that the size of Co₃O₄ domains in L_{0.9}CO is much larger than the Li/Co antisites domains in L_{0.9}M_{0.05}CO, illustrating the essential role of MgO on tuning the microscopic structure. Moreover, the content of Li/Co antisites in $L_{0.9}M_{0.05}CO$ is estimated to be $\approx 2.9\%$. The Li/Co antisites tend to enlarge the lattice value of c as compared with other three samples (Table S2, Supporting Information), which can facilitate Li⁺ ion diffusion inside the L_{0.9}M_{0.05}CO lattice.

TGA and DSC measurements are conducted to rationalize the influence of MgO on the bulk structure of $L_{0.9}M_{0.05}\text{CO}$ (Figure S7, Supporting Information). The formation reaction of LiCO_2 includes two steps: the decomposition of Li_2CO_3 ($\text{Li}_2\text{CO}_3 \rightarrow \text{Li}_2\text{O} + \text{CO}_2$) at $\approx\!550\text{--}650$ °C and the following reactions ($3\text{Li}_2\text{O} + 2\text{Co}_3\text{O}_4 + 0.5\text{O}_2 \rightarrow 6\text{Li}\text{CoO}_2$) at $\approx\!650\text{--}950$ °C. It can be seen that introduction of MgO leads to higher chemical reaction temperature, indicating the faster chemical reaction between the molten Li_2O and Co_3O_4 crystal, as well as the accelerated reaction rate for spinel-to-layer phase transition. As a consequence, only the Li/Co antisites are left in the bulk structure of $L_{0.9}M_{0.05}\text{CO}$, while Co_3O_4 domains are absent.

The Mg-rich surface layers also play crucial roles on enhancing the cycling stability of $L_{0.9}M_{0.05}CO$ at 4.6 V. Since the radius of Mg²⁺ ions (\approx 0.72 Å) is similar to that of the Li⁺ ions (\approx 0.76 Å), Mg²⁺ ions are prone to replace the Li sites in LiCoO₂, which can be regarded as another form of Mg in the electrode apart from that in the surface MgO layer.^[5a,7e] Based on the TEM and EDSmapping results (Figure 1e and Figure S8, Supporting Information), an obvious Mg-rich layer is detected covering the surface of L_{0.9}M_{0.05}CO, and clear lattice fringes of MgO crystal with a thickness of \approx 2 nm are observed.^[7c] In contrast, for L_{1.0}M_{0.05}CO sample, no visible Mg-rich layer and no lattice fringes of MgO crystal are found (Figure S3, Supporting Information). For L_{0.9}M_{0.05}CO, XPS results show the clear signals of Mg-O, and a Mg-pillar enriched surface with a thickness of \approx 30 nm (Figure 1g,h), which can potentially stabilize the surface structure under high state of charge (SOC). As compared with $L_{0.9}M_{0.05}CO$, Mg ions in L_{1.0}M_{0.05}CO tend to be uniformly distributed across the whole particle (Figure S9, Supporting Information). These results illustrate a scenario where both of the outermost Mg-O coating layer and the Mg-pillar enriched surface are preferentially formed upon Li deficiency, without which the Mg pillars would likely be scattering inside LiCoO₂. The Li deficiency contributes to the formation of Li/Co antisites to alleviate the Mg²⁺ diffusion from sur-

Sample	Structure feature
LCO	Pure layered structure
L _{0.9} CO	$\label{eq:comeco3O4} Some \ \mbox{Co}_3\ \mbox{O}_4 \ domains \ and \ \mbox{Li/Co} \ antisites \ in \ the \ layer structure \ substrate$
L _{1.0} M _{0.05} CO	Pure layered structure with uniformly distributed Mg pillars across the particle
L _{0.9} M _{0.05} CO	A combination of the bulk Li/Co antisites, the Mg-pillar enriched surface, and the outermost surface Mg-O layers

face into core, therefore, the Mg-pillar enriched surface and MgO coating is observed in $L_{0.9}M_{0.05}CO$.

Furthermore, we find that the surface Mg-O content in L_{0.9}M_{0.05}CO decreases with increasing synthesis temperature from 800 to 1000 °C (Figure S10, Supporting Information). This can be rationalized by that the higher sintering temperature can promote Mg penetration from surface into the interior of L_{0.9}M_{0.05}CO, leading to the decrease in surface Mg-O coating layer. Based on the electrochemical (EC) performances, the optimal sintering temperature is estimated to be ≈900 °C, at which a proper thickness of surface Mg-O layer (≈2 nm) and Mg-pillar enriched surface are preserved to ensure tough surface structure of $L_{0.9}M_{0.05}CO$. Overall, the structure features of LCO, L_{0.9}CO, L_{1.0}M_{0.05}CO, and L_{0.9}M_{0.05}CO are summarized in Table 1 (Figure 1a-d), which clarifies the significant impact of Li deficiency and MgO incorporation on the LiCoO₂ structure. For L_{0.9}M_{0.05}CO, a combination of the bulk Li/Co antisites, the Mg-pillar enriched surface, and the outermost MgO layer are integrated to boost the EC performance at 4.6 V, as demonstrated in Figure 1e-g.

2.2. Electrochemical Performance

The galvanostatic charge/discharge profiles and the corresponding dQ/dV curves of four electrodes are displayed in **Figure 2**a–d and Figures S11 and S12 (Supporting Information). For LCO, $L_{0.9}$ CO, and $L_{1.0}$ M $_{0.05}$ CO, the charge/discharge behaviors between the first and following cycles are nearly the same with gradually fading discharge capacity. However, for $L_{0.9}$ M $_{0.05}$ CO, the first charge curve shows greater polarization than the following cycles, and the discharge capacity gradually increases. That is to say, there exists a capacity activation process. Because the surface Mg–O layer is not an ideal Li⁺ ion conductor, a capacity activation process is needed to achieve an chemically interface evolution from MgO to compounds containing Li, Mg, Co, O, and F elements (Figure S13, Supporting Information), which facilitates the Li⁺ ion transport in the following cycles with suppressed Co dissolution and structure collapse.

Several important indices are employed to evaluate the EC performance in 3.0–4.6 V versus Li/Li⁺, including coulomb efficiency (CE) upon the first cycle at a current of 0.2 C (first CE), discharge capacity of the fifth cycle at 0.2 C (Cap. $_{0.2C}$), discharge rate capacity at 8 C (R-Cap. $_{8C}$), and capacity retention after 100 cycles at a current of 1 C (Cap.-Ret. $_{100\text{th}}$), as demonstrated in Figure 2e. The first CE of LCO, L $_{0.9}$ CO, L $_{1.0}$ M $_{0.05}$ CO,

16163028, 2023, 38, Downloaded

onlinelibrary, wiley, com/doi/10.1002/adfm.202302622 by University Town Of Shenzhen, Wiley Online Library on [23/11/2025]. See the Terms

nditions) on Wiley Online Library for rules of use; OA articles are governed by the applicable Creative Commons

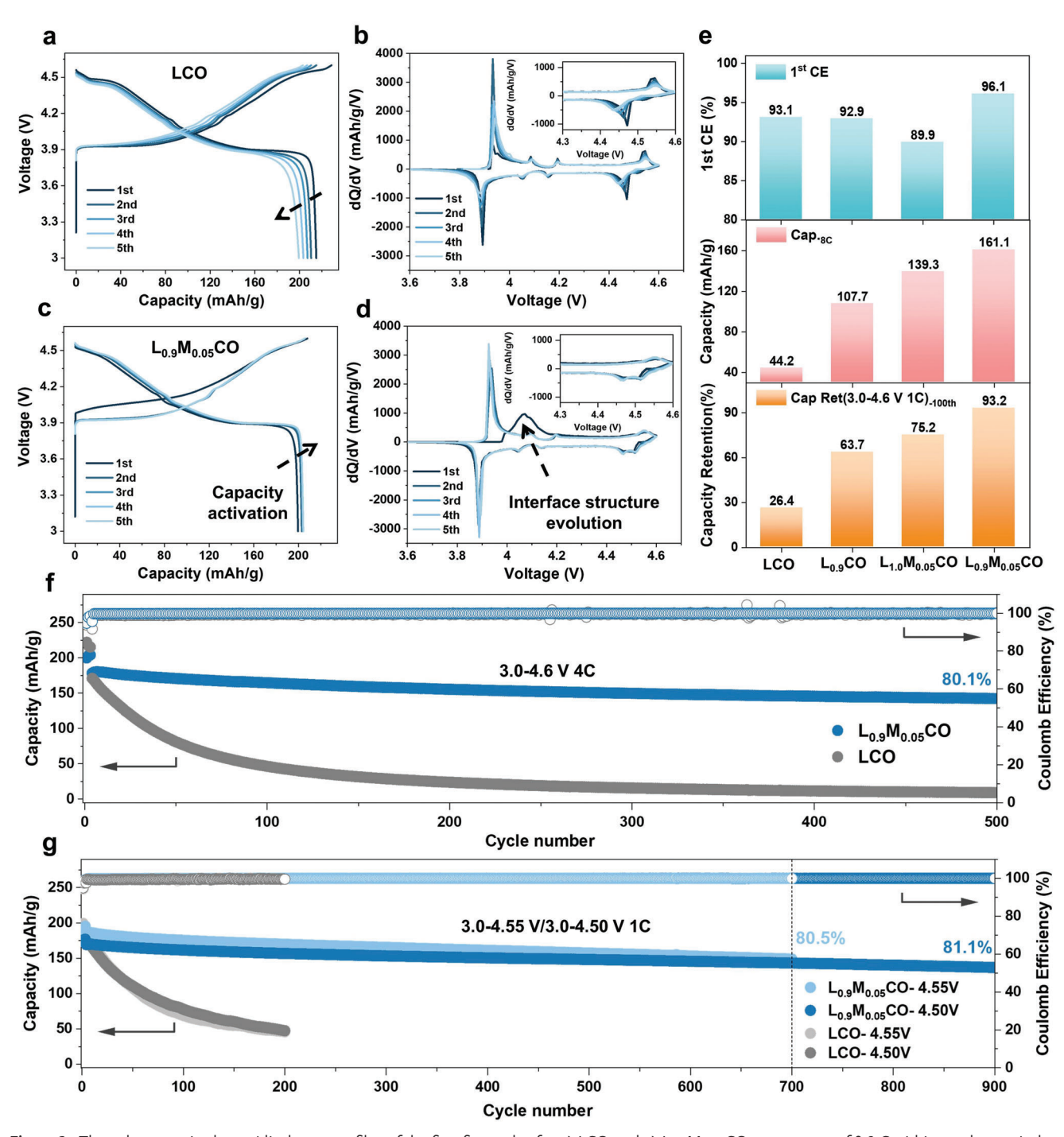


Figure 2. The galvanostatic charge/discharge profiles of the first five cycles for a) LCO and c) $L_{0.9}M_{0.05}CO$ at a current of 0.2 C within a voltage window of 3.0–4.6 V.The corresponding dQ/dV curves for b) LCO and d) $L_{0.9}M_{0.05}CO$. e) The CE upon the first cycle at 0.2 C (first CE), discharge rate capacity at 8 C (R-Cap._{8C}), and capacity retention after 100 cycles at 1C (Cap.-Ret._{100th}) for LCO, $L_{0.9}CO$, $L_{1.0}M_{0.05}CO$, and $L_{0.9}M_{0.05}CO$. f) Cycling performance at 4 C within a voltage window of 3.0–4.6 V for $L_{0.9}M_{0.05}CO$. g) Cycling performance at 1 C within a voltage window of 3.0–4.5 V for $L_{0.9}M_{0.05}CO$.

and $L_{0.9}M_{0.05}CO$ are $\approx 93.1\%$, $\approx 92.9\%$, $\approx 89.9\%$, and $\approx 96.1\%$, respectively. The value of the first CE represents the utilization degree of Li⁺ ions in the pristine electrode, which is a significant index for designing full-cells in industry. Higher value of the first CE means lower consumption of Li⁺ ions to form cathode/electrolyte interface (CEI) compounds. The highest first CE

of $L_{0.9}M_{0.05}CO$ indicates the highest Li^+ ion utilization, which is beneficial for cycling stability.

The Cap. $_{0.2C}$ values of LCO, $L_{0.9}$ CO, $L_{1.0}M_{0.05}$ CO, and $L_{0.9}M_{0.05}$ CO are \approx 199.4, \approx 206.5, \approx 199.8, and \approx 204.5 mAh g $^{-1}$, respectively. Both the Cap.-Ret. $_{8C}$ and the Cap.-Ret. $_{100}$ values are increasing in the sequence from LCO to $L_{0.9}M_{0.05}$ CO. These results

16163028, 2023, 38, Downloaded from https://advanced.onlinelibrary.wiley.com/doi/10.1002/adfm.202302622 by University Town Of Shenzhen, Wiley Online Library on [23/11/2025]. See the Terms and Conditions (https://onlinelibrary.wiley.com/derms

and-conditions) on Wiley Online Library for rules of use; OA articles are governed by the applicable Creative Commons

Table 2. Structure features after first charge to 4.6 V versus Li/Li⁺.

Sample	Structure feature
LCO	Thick surface spinel phase, and bulk layer structure
L _{0.9} CO	Thick surface spinel phase and bulk spinel/layer hybrid structure with high degree of lattice distortion
L _{1.0} M _{0.05} CO	Thick surface spinel phase and bulk spinel/layer hybrid structure
L _{0.9} M _{0.05} CO	Well-maintained layered structure with bulk Li/Co antisites and surface Mg-pillars

indicate that L_{0.9}M_{0.05}CO shows the optimal overall EC performance, including considerable reversible discharge capacity, the best rate and cycling performance, and the highest Li+ ion utilization. Besides, as compared with other samples, L_{0.9}M_{0.05}CO shows the obviously enhanced diffusion kinetics, as illustrated by GITT results (Figure S14, Supporting Information), which is mainly due to its optimized surface/bulk structures. The novel structures of the bulk Li/Co antisites and Mg-rich surface of $L_{0.9}M_{0.05}CO$ contribute to the rapid Li^+ ion diffusion inside the lattice, resulting in the enhanced diffusion kinetics. L_{0.9}M_{0.05}CO also displays a high capacity retention of >85% after 200 cycles in 3.0-4.6 V versus Li/Li⁺ at 1 C, >80% after 500 cycles in 3.0-4.6 V at 4 C, >80% after 700 cycles in 3.0-4.55 V at 1 C, and >80% after 900 cycles in 3.0-4.5 V at 1 C (Figure 2e-g). Besides, the excellent cycle performance of the pouch type full-cell with L_{0.9}M_{0.05}CO as cathode, and graphite as the anode is presented in Figure S15 (Supporting Information), which not only justifies the beneficial effects of the multiple structure modulation, but also provides huge potential for industrial application of the L_{0.9}M_{0.05}CO electrode. In Table S7 (Supporting Information), we also list the EC performance comparison of different kinds of Mg modified LCO at the high charging cutoff voltage, which shows that one-step sintering L_{0.9}M_{0.05}CO has a competitive performance.

2.3. Li/Co Antisites and Mg Pillars

To unravel the origin of improved electrochemical performance of L_{0.9}M_{0.05}CO sample, the structural evolution of bulk and surface in the first cycle is further investigated. We find that LCO, L_{0.9}CO, L_{1.0}M_{0.05}CO, and L_{0.9}M_{0.05}CO display different behavior of structural evolution in the first cycle, especially after the first charge to 4.6 V versus Li/Li+, as demonstrated by TEM results (Figure S16, Supporting Information). The detailed results are summarized and compared in Table 2. Notably, after the first charge, a thick phase transition layer composed of spinel phase emerges in the surface region of LCO, $L_{0.9}$ CO, and $L_{1.0}M_{0.05}$ CO, indicating that the unsatisfactory cycling performance of these samples originates from the fragile surface under high SOC. On the contrary, for L_{0.9}M_{0.05}CO, the surface structure is well maintained after the first charge to 4.6 V, which clearly shows the stabilizing effect of the outermost Mg-O layer and Mg-pillar enriched surface on the electrode surface. We further compare the TEM results after the first discharge, as shown in Figure S17 (Supporting Information). For LCO, the outermost rock salt phase and surface spinel phase are preserved, with some nanocracks detected in the bulk region, indicating the poor phase reversibility. For

 $\rm L_{0.9}M_{0.05}CO$, the surface and bulk phase structures remain nearly unchanged, showing the highly reversible phase transition upon cycle.

Apart from the well-maintained surface structure, the reversibility of bulk structural evolution is also significant for longterm cyclic performances. dQ/dV curves show the phase transition of LiCoO2 under different voltage ranges, including solid solution reaction in 3.8-4.0 V, two-phase transition region (hexagonal/monoclinic/hexagonal phase transitions) in 4.0-4.2 V, and O3/H1-3 phase transition in 4.4-4.6 V (Figure 2b,d; Figure S11, Supporting Information). Among them, the O3/H1-3 phase transition plays the most significant impact on the cycling stability at 4.6 V. We find that upon cycling, the LCO and L_{1.0}M_{0.05}CO samples with pure layer structure show poor reversibility of O3/H1-3 phase transition, while L_{0.9}CO with Co₃O₄ domains in layer structure displays much superior reversibility. Surprisingly, the O3/H1-3 phase transition in $L_{0.9}M_{0.05}CO$ with bulk Li/Co antisites and Mg-rich surface is not only highly reversible but also significantly depressed. Both the bulk Li/Co antisites and Co₃O₄ domains tend to enhance the reversibility of O3/H1-3 phase transition, and at the same time, the Mg pillars, either uniformly distributed or surface enriched, can reduce the degree of O3/H1-3 phase transition, which has never been reported in previous stud-

The comparison of in situ XRD patterns in the initial two cycles are further illustrated in Figure 3a,b and Figure S18 (Supporting Information). The lattice evolution is similar for all electrodes, but with different lattice variation values, which is reflected by the (003) peaks. For the shift of (003) peak position $(\Delta_{2\theta})$ for LCO, $L_{0.9}$ CO, $L_{1.0}M_{0.05}$ CO, and $L_{0.9}M_{0.05}$ CO are 1.307°, 1.226°, 1.165°, and 0.939°, respectively. $L_{0.9}M_{0.05}CO$ shows the smallest $\Delta_{2\theta}$ mainly due to the reduced degree of O3/H1-3 phase transition. This can be further verified by the ex situ XRD patterns of LCO and L_{0.9}M_{0.05}CO (Figure 3c,d). For LCO at fully charged state, only one peak of the H1-3 phase appears, while for $L_{0.9}M_{0.05}CO$ at fully charged state, the peaks for both O3 and H1-3 phases are observed, indicating an incomplete phase transition with a large fraction of O3 phase remaining. Meanwhile, when LCO is charged to 4.6 V again, the shift of (003) peak position ($\Delta_{2\theta}$) and the intensity of H1-3 peak reduce significantly, which indicate the partial collapse of the structure.

Notably, L_{0.9}M_{0.05}CO shows reduced and reversible O3/H1-3 phase transition, which is correlated with both the bulk Li/Co antisites and the Mg-pillar enriched surface. We employed density functional theory (DFT) calculations to rationalize the underlying mechanism. Given that the H1-3 phase is essentially an intermixing of both O3 and O1 phases in an ordered configuration, [16] the O3/H1-3 phase transition can thus be regarded as an intermediate process of O3/O1 phase transition. This process corresponds to the sliding of O-Co-O layer when most of the Li ions are extracted from the adjacent Li layers. To simplify the calculations, we consider the energy consumption for the transition from O3 to O1 phase, which can dictate the thermodynamic driving force for O3/H1-3 phase transition. We investigate the case of Li/Co antisites with a high local concentration. The concentrated Li/Co antisites in O3 phase can lead to the formation of spinel phase, which proceeds by orderly exchanging the positions of one fourth of Co ions with the Li ions nearby.[17] Therefore, the O sublattices in O3 and spinel phases are coherent, and we constructed

www.advancedsciencenews.com

16163028, 2023, 38, Downloaded

onlinelibrary, wiley, com/doi/10.1002/adfm.202302622 by University Town Of Shenzhen, Wiley Online Library on [23/11/2025]. See the Terms

on Wiley Online Library for rules of use; OA articles are governed by the applicable Creative Commons

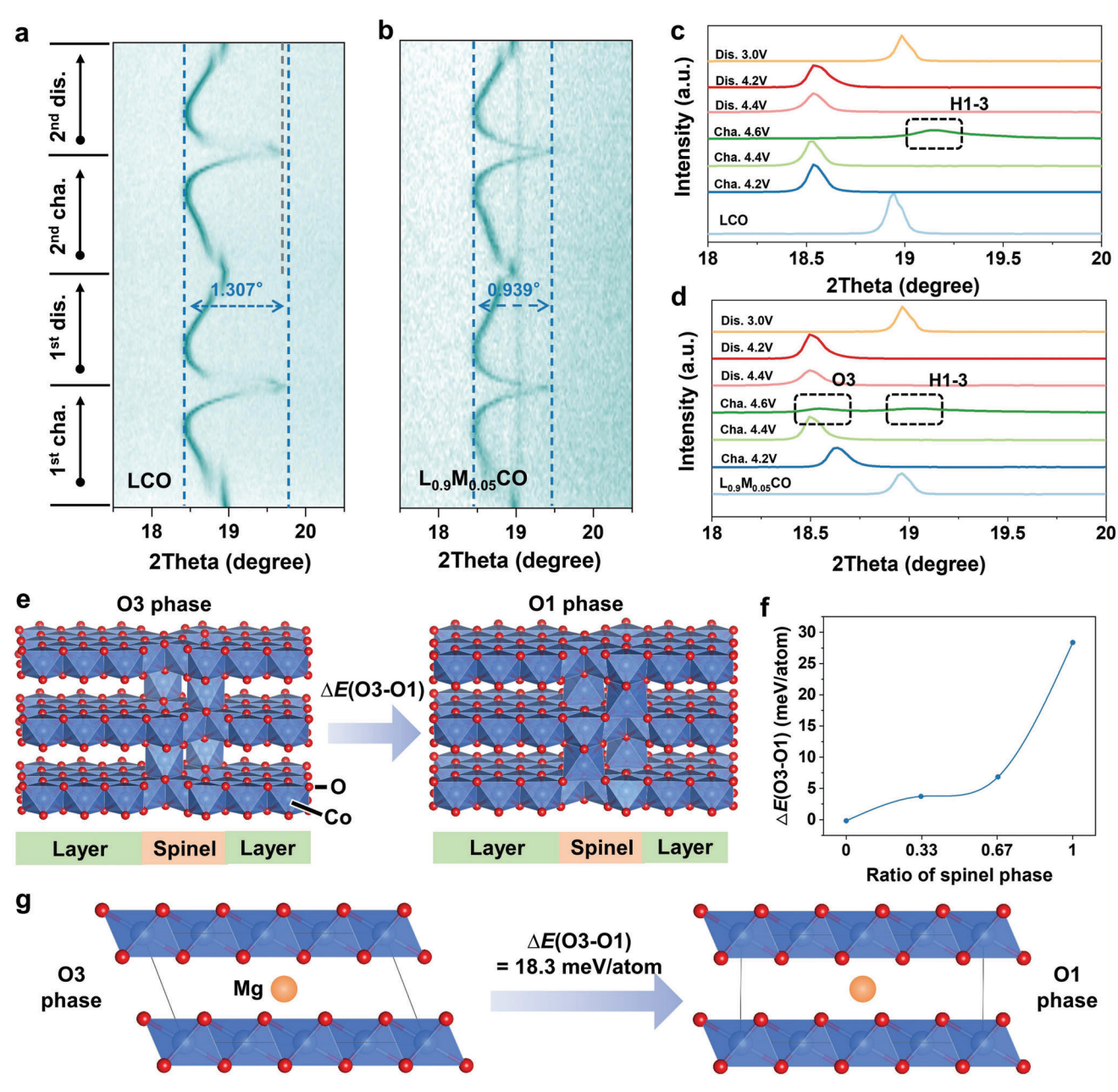


Figure 3. The in situ XRD patterns collected within a voltage window of 3.0–4.6 V for the first two cycles at 0.2 C: a) LCO and b) $L_{0.9}M_{0.05}CO$. The ex situ XRD patterns collected within a voltage window of 3.0-4.6 V for the first cycle at 0.2 C: c) LCO and d) L_{0.9} M_{0.05}CO. e) The structure illustration for O3/O1 phase transition of layered LiCoO₂ with substantial Li/Co antisite (spinel phase). f) The energy change in O3/O1 phase transition (ΔE (O3-O1)) as a function of the ratio of spinel phase in the model. g) The structure illustration for O3/O1 phase transition of Mg-pillared layered LiCoO2.

such coherent model to evaluate the influence of substantial Li/Co antisites on phase transition (Figure 3e). All the Li ions are extracted to simulate the fully charged state of the electrode. As compared to the pristine LiCoO₂ that exhibits negative value (-0.2 meV/atom) for the energy change in O3/O1 phase transition (ΔE (O3-O1)), the incorporation of coherent spinel phase in the lattice increases this energy change to positive values (Figure 3f), suggesting higher stability for the O3 phase than O1 phase. This would mean that there is no thermodynamic driving force for O3/O1 phase transition, nor for O3/H1-3. As in the

Adv. Funct. Mater. 2023, 33, 2302622

real case there are still regions with low concentrations of Li/Co antisites, the O3/H1-3 phase transition cannot be eliminated in the entire electrode. Yet, from the above results we can safely attribute the reduced degree of O3/H1-3 transition in L_{0.9}M_{0.05}CO to the pronounced Li/Co antisites in the lattice.

We further evaluate the effect of Mg pillars on the phase transition of the layer structure. According to the above discussion, the propensity for O3/H1-3 phase transition can be estimated from the energy change in O3/O1 phase transition (ΔE (O3-O1)). We consider the case where a single Mg ion is left in the Li layer

16163028, 2023, 38, Downloaded from https://advanced.onlinelibrary.wiley.com/doi/10.1002/adfm.202302622 by University Town Of Shenzhen, Wiley Online Library on [23/11/2025]. See the Terms and Conditions (https://onlin

conditions) on Wiley Online Library for rules of use; OA articles are governed by the applicable Creative Commons

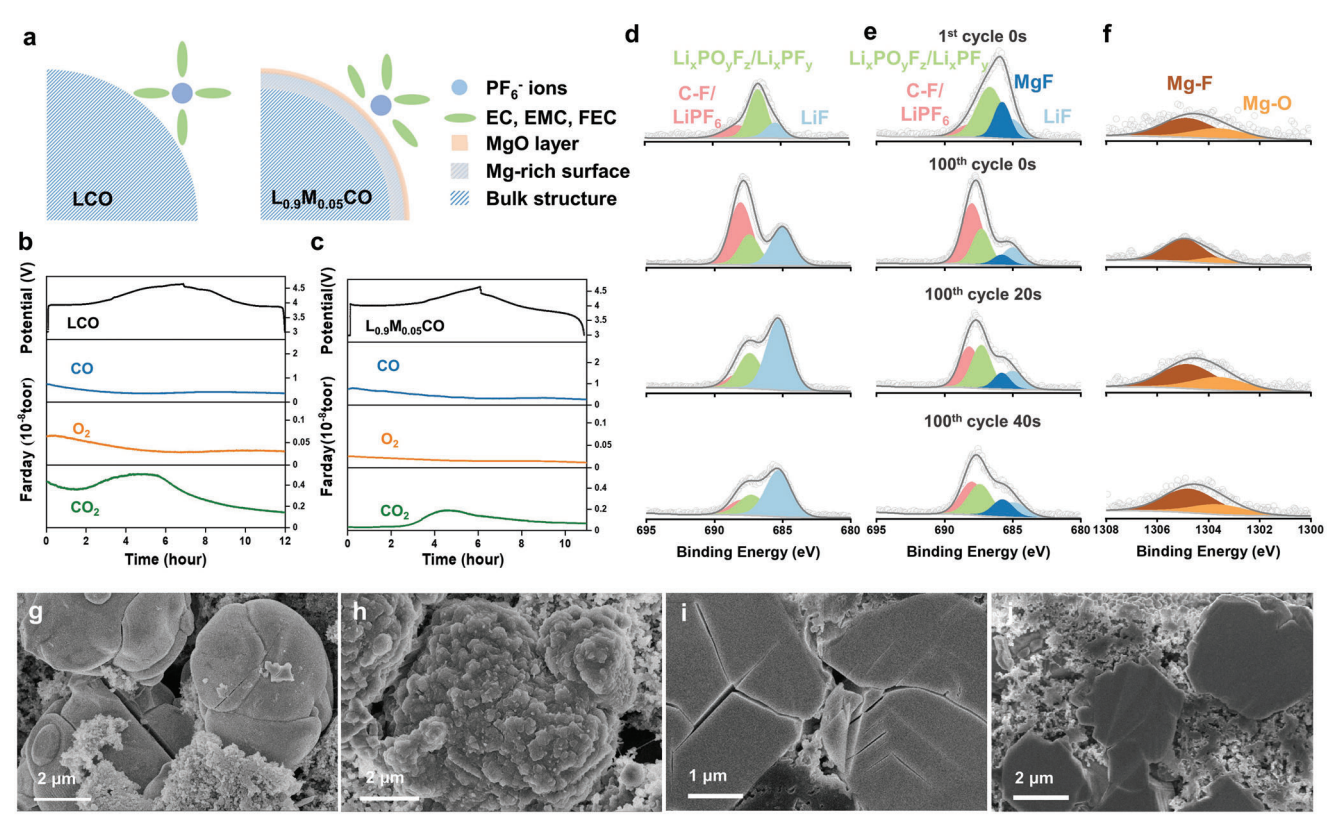


Figure 4. a) Schematic illustration of different species adsorbed on surface in the Helmholtz layer for LCO and $L_{0.9}M_{0.05}CO$. In situ DEMS measurement of b) LCO and c) $L_{0.9}M_{0.05}CO$ within a voltage window of 3.0–4.6 V for the first cycle at 0.2 C. XPS spectra of O_{1s} for d) LCO, e) $L_{0.9}M_{0.05}CO$, and Mg_{1s} for f) $L_{0.9}M_{0.05}CO$ after one cycle at 0.2 C and 100 cycles at 1 C. SEM and cross-section SEM images of g,i) LCO and h,j) $L_{0.9}M_{0.05}CO$ after 100 cycles at 1 C.

occupying the octahedral site while all Li ions are extracted (Figure 3g). The ΔE (O3-O1) reaches 18.3 meV/atom, suggesting high energy penalty for this phase transition. Similar to Li/Co antisites, the Mg pillars in the layer structure can contribute to a reduced degree of O3/H1-3 phase transition and result in a promoted reversibility in electrochemical cycling.

2.4. Long-Term Cycle Evaluation

For LiCoO $_2$ cathode cycling at 3.0–4.6 V versus Li/Li $^+$, all the capacity fading issues, including surface deterioration, bulk phase transition, formation of cracks or voids, etc., are closely related with the evolution of the surface. At charged state, the lithium salt (LiPF $_6$) and solvents (EC, EMC, and FEC) in electrolyte react with the highly oxidative cathode, leading to the CEI formation, which significantly affects the interface charge/mass transfer process upon cycling. To enhance the cycling stability, the CEI must be mechanically tough, chemically stable, as well as evenly and completely covered on the particle surface.

For $L_{0.9}M_{0.05}CO$, the Mg-rich surface modulates the surface adsorption state upon charging, resulting in more PF_6^- and less solvents adsorbed on surface in the Helmholtz layer (**Figure 4a**). As a result, more PF_6^- solvents participate in the interface reaction, rather than the solvents, leading to reduced release of CO_2 and O_2 caused by Co^{4+} and O^{n-} species, $S^{[8a]}$ and forming reaction

products related with PF $_6$ on the surface of L $_{0.9}$ M $_{0.05}$ CO, as testified by DEMS results (Figure 4b,c). The CEI of L $_{0.9}$ M $_{0.05}$ CO shows a MgF-rich feature, which is composed of the inorganic MgF, MgO, LiF, Li $_x$ PF $_y$ O $_z$, and Li $_x$ PF $_y$, and remains nearly unchanged from the 1st to 100th cycle (Figure 4e,f and Figure S20b, Supporting Information). [19] Meanwhile, this MgF-rich CEI is fully covered on the particle surface (Figure 4h; Figure S19c,d, Supporting Information), showing a high chemical stability. [19b,20] However, for LCO, the LiF content in CEI increases obviously from 1st to 100th cycle (Figure 4d; Figure S20a, Supporting Information), and the CEI is not fully covered on particle surface (Figure 4g; Figure S19a,b, Supporting Information), indicating the unstable nature.

The MgF-rich CEI not only provides a full coverage to protect $L_{0.9}M_{0.05}CO$ from further side reactions, but also play significant role on enhancing the Li⁺ ion insertion/extraction homogeneity, as discussed in the subsequent paragraph. Due to this high Li⁺ ion insertion/extraction homogeneity, no crack is observed in $L_{0.9}M_{0.05}CO$ and the (003) peak position is nearly unchanged after 100 cycles (Figure 4j and Figure S21b, Supporting Information), which well guarantees the particle integrity. However, extensive cracks are progressively formed in LCO (Figure 4g,i), which tears the particle into fragments and greatly deteriorates the electrode performance. Meanwhile, the (003) peak of LCO moves toward lower degree, confirming the severe structural deformation (Figure S21a, Supporting Information). Furthermore,

16163028, 2023, 38, Downloaded

.com/doi/10.1002/adfm.202302622 by University Town Of Shenzhen, Wiley Online Library on [23/11/2025]. See the Terms

onditions) on Wiley Online Library for rules of use; OA articles are governed by the applicable Creative Commons

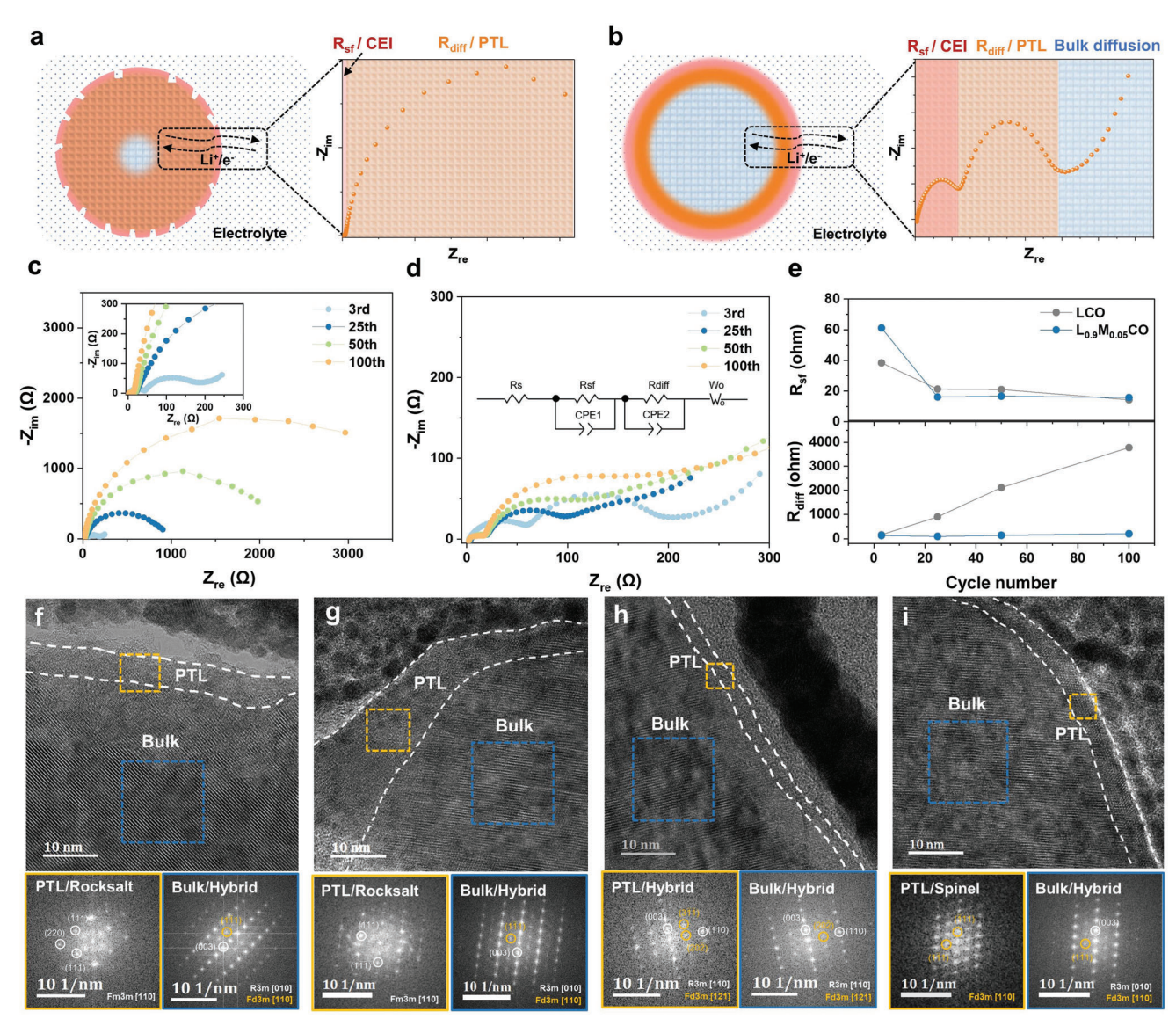


Figure 5. a) Schematic illustration of the structure from surface to interior for a) LCO and b) $L_{0.9}M_{0.05}CO$ after 25 cycles at 1 C. Electrochemical impedance spectra (EIS) of c) LCO and d) $L_{0.9}M_{0.05}CO$ after three cycles at 0.2 C, 25, 50, and 100 cycles at 1 C. e) The corresponding fitting results of $R_{\rm sf}$ and $R_{\rm diff}$ by equivalent circuit. HRTEM image of bulk and surface structure and corresponding FFT image of f) LCO after one cycle at 0.2 C, g) LCO after 100 cycles at 1 C. h) $L_{0.9}M_{0.05}CO$ after one cycle at 0.2 C and i) $L_{0.9}M_{0.05}CO$ after 100 cycles at 1 C.

some cracks are also detected in $L_{0.9}CO$ and $L_{1.0}M_{0.05}CO$ after 100 cycles (Figure S22, Supporting Information); that is to say, only the pure bulk phase modulation or the uniformly distributed Mg-pillars in layer structure substrate is not eligible to suppress the crack formation, which indicates the significant role of the multiple modulation, including both the bulk Li/Co antisites and the Mg-rich surface, on maintaining the particle integrity of $L_{0.9}M_{0.05}CO$ upon long-term cycling.

EIS results are conducted to analyze the enhanced cycle stability of $L_{0.9}M_{0.05}CO$ from a more microscopic perspective. We observe that, upon cycling, the cathode structure from surface to interior includes the outermost CEI, the surface phase transition layer (PTL), and the bulk structure (**Figure 5**a,b). Generally, during discharge, Li⁺ ions diffuse successively across the CEI and

the PTL, finally enter into the bulk structure, and vice versa for the charge process. As reflected in a typical EIS plots, there exist two impedance semicircles and one diffusion tail corresponding to the surface film resistance ($R_{\rm sf}$) related with CEI, the diffusion resistance ($R_{\rm diff}$) across the PTL, as well as further Li⁺ ion diffusion inside the bulk lattice structure, respectively. Among which, the physical meaning of the $R_{\rm diff}$ equals to the charge transfer resistance ($R_{\rm ct}$) in previous reports. [6b,7e,18c] In the case of highly deteriorated cathode, such as for the LCO after 25 cycles, due to the huge $R_{\rm diff}$ value for the PTL, only one impedance semicircle corresponding to $R_{\rm sf}$ and one incomplete semicircle representing $R_{\rm diff}$ is observed (Figure 5a).

Figure 5c,d shows the EIS plots of LCO and $L_{0.9}M_{0.05}CO$ after the 3rd, 25th, 50th, and 100th cycle, respectively. By fitting



www.advancedsciencenews.com

www.afm-journal.de

ADVANCED FUNCTIONAL MATERIALS 16163028, 2023, 38, Downloaded from https://advanced.onlinelibrary.wiley.com/doi/10.1002/adfm.202302622 by University Town Of Shenzhen, Wiley Online Library on [23/11/2025]. See the Terms

and-conditions) on Wiley Online Library for rules of use; OA articles are governed by the applicable Creative Commons License

the EIS plots, the surface film resistance $R_{\rm sf}$ and the diffusion resistance $R_{\rm diff}$ are obtained. Herein, the $R_{\rm sf}$ value is closely related with the CEI property, and the $R_{\rm diff}$ value corresponds to the Li⁺ ion diffusion across the PTL. The fitting results are shown in Figure 5e. Notably, the most significant difference lies in the $R_{\rm diff}$ value, which grows rapidly from 153 to 3776 Ω in 100 cycles for LCO, and keeps nearly unchanged in 100 cycles for L_{0.9}M_{0.05}CO. This comparison clearly indicates the pronounced structure toughness of L_{0.9}M_{0.05}CO due to the multiple modulations. Besides, the above results further demonstrate the advantages of EIS method in revealing the essence of high stability of high-voltage LiCoO₂ materials, especially in long-term cycles.

TEM is utilized to reveal the surface structure of LCO and $L_{0.9}M_{0.05}$ CO upon cycling. We note that the CEI film is damaged during the FIB cutting, which makes it difficult to be observed under TEM. Here, the PTL and bulk information of LCO and $L_{0.9}M_{0.05}$ CO after the 1st and 100th cycle are provided and compared. For LCO, an obvious PTL layer forms since the first cycle with a surface rock salt phase of ≈ 10 nm, which progressively increases in 100 cycles (Figure 5f,g), while for $L_{0.9}M_{0.05}$ CO, the PTL shows a spinel-like phase layer of <5 nm, rather than the thick and electrochemically inert rock salt phase, and the PTL thickness remains nearly unchanged in 100 cycles. This PTL is not only tough enough to maintain the surface structure, but also provides sufficient Li⁺ ion diffusion pathways leading to the low $R_{\rm diff}$ value in $L_{0.9}M_{0.05}$ CO.

Overall, the Mg-rich surface contributes to the formation of a highly stable and protective CEI, which is fully covered on $L_{0.9}M_{0.05}\text{CO}$ surface, and effectively suppresses the crack formation via improving the Li+ ion insertion/extraction homogeneity. Moreover, the Mg-pillar enriched surface plays a beneficial role on mitigating the thickening and spreading of the PTL from surface into interior region upon long-term cycling, which makes the bulk structure of $L_{0.9}M_{0.05}\text{CO}$ always maintain an efficient Li+ ion host framework even after long-term cycles at 4.6 V.

3. Conclusion

In summary, we report a simple one-step synthesize method to achieve the multiple structure modulations of $L_{0.9}M_{0.05}CO$, which effectively enhanced the rate and cycle performances at 4.6 V. The structure modulations include the bulk Li/Co antisites, the Mg-pillar enriched surface, and the outermost MgO layer, among which the application of bulk Li/Co antisites to enhance the bulk structure stability of L_{0.9}M_{0.05}CO is firstly reported in literature. Due to these structure modulations, a reduced but reversible O3/H1-3 phase transition is achieved for L_{0.9}M_{0.05}CO, as illustrated by comparing the dQ/dV curves and the in situ XRD results, which is regarded as the structural origin for the excellent cycling stability at 4.6 V. Furthermore, we analyze the structural and electrochemical evolution of $\rm L_{0.9}M_{0.05}CO$ upon long-term cycling. The results indicate that the outermost Mg-O layer contributes to the formation of a protective and fully covered CEI on L_{0.9}M_{0.05}CO surface, which plays the role of suppressing both the side reactions and crack formation, and the Mg-pillar enriched surface helps to stabilize the surface structure via mitigating the thickening and spreading of the PTL from surface into interior upon long-term cycling. The mechanistic understanding obtained in this work can pave the way toward rational design of advanced cathode materials for Li-ion batteries.

Supporting Information

Supporting Information is available from the Wiley Online Library or from the author.

Acknowledgements

H.R. and W.Z. contributed equally to this work. This work was financially supported by the National Natural Science Foundation of China (52102201), Basic and Applied Basic Research Foundation of Guangdong Province (No. 2021B1515130002), and Soft Science Research Project of Guangdong Province (No. 2017B030301013).

Conflict of Interest

The authors declare no conflict of interest.

Data Availability Statement

Research data are not shared.

Keywords

LiCoO₂, Li/Co antisites, Mg pillars, Mg-O coating, Li-ion batteries

Received: March 7, 2023 Revised: April 13, 2023 Published online: May 26, 2023

- [1] Q. Liu, X. Su, D. Lei, Y. Qin, J. Wen, F. Guo, Y. A. Wu, Y. Rong, R. Kou, X. Xiao, F. Aguesse, J. Bareno, Y. Ren, W. Lu, Y. Li, *Nat. Energy* 2018, 3, 936.
- [2] S. Li, Y. Sun, A. Gao, Q. Zhang, X. Lu, X. Lu, Proc. Natl. Acad. Sci. USA 2022, 119, e2120060119.
- [3] a) Y. Lyu, X. Wu, K. Wang, Z. Feng, T. Cheng, Y. Liu, M. Wang, R. Chen, L. Xu, J. Zhou, Y. Lu, B. Guo, Adv. Energy Mater. 2021, 11, 2000982; b)
 J.-N. Zhang, Q. Li, C. Ouyang, X. Yu, M. Ge, X. Huang, E. Hu, C. Ma, S. Li, R. Xiao, W. Yang, Y. Chu, Y. Liu, H. Yu, X.-Q. Yang, X. Huang, L. Chen, H. Li, Nat. Energy 2019, 4, 594.
- [4] a) S. Kalluri, M. Yoon, M. Jo, S. Park, S. Myeong, J. Kim, S. X. Dou, Z. Guo, J. Cho, Adv. Energy Mater. 2017, 7, 1601507; b) K. Wang, J. Wan, Y. Xiang, J. Zhu, Q. Leng, M. Wang, L. Xu, Y. Yang, J. Power Sources 2020, 460, 228062.
- [5] a) Y. Huang, Y. Zhu, H. Fu, M. Ou, C. Hu, S. Yu, Z. Hu, C.-T. Chen, G. Jiang, H. Gu, H. Lin, W. Luo, Y. Huang, Angew. Chem., Int. Ed. 2021, 60, 4682; b) W. Kong, J. Zhang, D. Wong, W. Yang, J. Yang, C. Schulz, X. Liu, Angew. Chem., Int. Ed. 2021, 60, 27102; c) J. Chen, H. Chen, S. Zhang, A. Dai, T. Li, Y. Mei, L. Ni, X. Gao, W. Deng, L. Yu, G. Zou, H. Hou, M. Dahbi, W. Xu, J. Wen, J. Alami, T. Liu, K. Amine, X. Ji, Adv. Mater. 2022, 34, 2204845; d) A. Fu, Z. Zhang, J. Lin, Y. Zou, C. Qin, C. Xu, P. Yan, K. Zhou, J. Hao, X. Yang, Y. Cheng, D.-Y. Wu, Y. Yang, M.-S. Wang, J. Zheng, Energy Storage Mater. 2022, 46, 406; e) J. Xia, N. Zhang, Y. Yang, X. Chen, X. Wang, F. Pan, J. Yao, Adv. Funct. Mater. 2022, 33, 2212869.



www.advancedsciencenews.com



16163028, 2023, 38, Downloaded from https://advanced.onlinelibrary.wiley.com/doi/10.1002/adfm.202302622 by University Town Of Shenzhen, Wiley Online Library on [23/11/2025]. See the Terms

and Conditions

and-conditions) on Wiley Online Library

of use; OA articles are governed by the applicable Creative Commons

www.afm-journal.de

- [6] a) H. J. Lee, J. H. Lee, I. H. Son, S. Han, P. Byeon, M.-S. Park, S.-Y. Chung, J. W. Choi, ACS Appl. Energy Mater. 2018, 1, 5726; b) J.-H. Shim, K.-S. Lee, A. Missyul, J. Lee, B. Linn, E. C. Lee, S. Lee, Chem. Mater. 2015, 27, 3273; c) M.-J. Lee, S. Lee, P. Oh, Y. Kim, J. Cho, Nano Lett. 2014, 14, 993; d) X. Tan, T. Zhao, L. Song, D. Mao, Y. Zhang, Z. Fan, H. Wang, W. Chu, Adv. Energy Mater. 2022, 12, 2200008; e) T. Cheng, Z. Ma, R. Qian, Y. Wang, Q. Cheng, Y. Lyu, A. Nie, B. Guo, Adv. Funct. Mater. 2021, 31, 2001974; f) Y. Wang, Q. Zhang, Z.-C. Xue, L. Yang, J. Wang, F. Meng, Q. Li, H. Pan, J.-N. Zhang, Z. Jiang, W. Yang, X. Yu, L. Gu, H. Li, Adv. Energy Mater. 2020, 10, 2001413.
- [7] a) T. Fan, Y. Wang, V. K. Harika, A. Nimkar, K. Wang, X. Liu, M. Wang, L. Xu, Y. Elias, H. Scalar, M. S. Chae, Y. Min, Y. Lu, N. Shpigel, D. Aurbach, Adv. Sci. 2022, 9, 2202627; b) J.-H. Shim, S. Lee, S. S. Park, Chem. Mater. 2014, 26, 2537; c) N. Taguchi, T. Akita, K. Tatsumi, H. Sakaebe, J. Power Sources 2016, 328, 161; d) T. Cheng, Q. Cheng, Y. He, M. Ge, Z. Feng, P. Li, Y. Huang, J. Zheng, Y. Lyu, B. Guo, ACS Appl. Mater. Interfaces 2021, 13, 42917; e) Y. Orikasa, D. Takamatsu, K. Yamamoto, Y. Koyama, S. Mori, T. Masese, T. Mori, T. Minato, H. Tanida, T. Uruga, Z. Ogumi, Y. Uchimoto, Adv. Mater. Interfaces 2014, 1, 1400195; f) X. Yang, C. Wang, P. Yan, T. Jiao, J. Hao, Y. Jiang, F. Ren, W. Zhang, J. Zheng, Y. Cheng, X. Wang, W. Yang, J. Zhu, S. Pan, M. Lin, L. Zeng, Z. Gong, J. Li, Y. Yang, Adv. Energy Mater. 2022, 12, 2200197.
- [8] a) W. Huang, Q. Zhao, M. Zhang, S. Xu, H. Xue, C. Zhu, J. Fang, W. Zhao, G. Ren, R. Qin, Q. Zhao, H. Chen, F. Pan, Adv. Energy Mater.
 2022, 12, 2200813; b) Z. Zhu, H. Wang, Y. Li, R. Gao, X. Xiao, Q. Yu, C. Wang, I. Waluyo, J. Ding, A. Hunt, J. Li, Adv. Mater. 2020, 32, 2005182; c) S. Mao, Z. Shen, W. Zhang, Q. Wu, Z. Wang, Y. Lu, Adv. Sci. 2022, 9, 2104841.
- [9] J. Li, C. Lin, M. Weng, Y. Qiu, P. Chen, K. Yang, W. Huang, Y. Hong, J. Li, M. Zhang, C. Dong, W. Zhao, Z. Xu, X. Wang, K. Xu, J. Sun, F. Pan, Nat. Nanotechnol. 2021, 16, 599.
- [10] S. Li, K. Li, J. Zheng, Q. Zhang, B. Wei, X. Lu, J. Phys. Chem. Lett. 2019, 10, 7537.

- [11] S. Xu, X. Tan, W. Ding, W. Ren, Q. Zhao, W. Huang, J. Liu, R. Qi, Y. Zhang, J. Yang, C. Zuo, H. Ji, H. Ren, B. Cao, H. Xue, Z. Gao, H. Yi, W. Zhao, Y. Xiao, Q. Zhao, M. Zhang, F. Pan, *Angew. Chem., Int. Ed.* 2023, 62, e202218595.
- [12] Z. Zhu, D. Yu, Z. Shi, R. Gao, X. Xiao, I. Waluyo, M. Ge, Y. Dong, W. Xue, G. Xu, W.-K. Lee, A. Hunt, J. Li, Energy Environ. Sci. 2020, 13, 1865.
- [13] J. Liu, J. Wang, Y. Ni, J. Liu, Y. Zhang, Y. Lu, Z. Yan, K. Zhang, Q. Zhao, F. Cheng, J. Chen, Angew. Chem., Int. Ed. 2022, 61, e202207000.
- [14] a) L. Wang, J. Ma, C. Wang, X. Yu, R. Liu, F. Jiang, X. Sun, A. Du, X. Zhou, G. Cui, Adv. Sci. 2019, 6, 1900355; b) J.-H. Shim, J.-M. Han, J.-H. Lee, S. Lee, ACS Appl. Mater. Interfaces 2016, 8, 12205.
- [15] a) S. A. Wicker, E. H. Walker Jr., Inorg. Chem. 2013, 52, 1772; b) J. Gim, Y. Zhang, H. Gao, G.-L. Xu, F. Guo, Y. Ren, K. Amine, Z. Chen, J. Power Sources 2020, 469, 228422; c) Y. Kan, Y. Hu, Y. Ren, J. Bareno, I. Bloom, Y.-K. Sun, K. Amine, Z. Chen, J. Power Sources 2014, 271, 97.
- [16] a) A. Van der Ven, M. K. Vydinol, G. Cedar, J. Electrochem. Soc. 1998, 145, 2149; b) Z. H. Chen, Z. H. Lu, J. R. Dahn, J. Electrochem. Soc. 2002, 149, A1604.
- [17] R. J. Gummow, D. C. Liles, M. M. Thackeray, *Mater. Res. Bull.* 1993, 28, 235.
- [18] a) P. Bai, X. Ji, J. Zhang, W. Zhang, S. Hou, H. Su, M. Li, T. Deng, L. Cao, S. Liu, X. He, Y. Xu, C. Wang, Angew. Chem., Int. Ed. 2022, 134, e202202731; b) J. Zhang, P.-F. Wang, P. Bai, H. Wan, S. Liu, S. Hou, X. Pu, J. Xia, W. Zhang, Z. Wang, B. Nan, X. Zhang, J. Xu, C. Wang, Adv. Mater. 2022, 34, 2204845; c) A. Yano, N. Taguchi, H. Kanzaki, M. Shikano, H. Sakaebe, J. Electrochem. Soc. 2021, 168, 050517.
- [19] a) Y.-C. Lu, A. N. Mansour, N. Yabuuchi, Y. Shao-Horn, Chem. Mater. 2009, 21, 4408; b) H. G. Kim, Y. J. Park, ACS Appl. Energy Mater. 2021, 4, 8220
- [20] Y. Bai, K. Jiang, S. Sun, Q. Wu, X. Lu, N. Wan, Electrochim. Acta 2014, 134, 347.